ELSEVIER

Earth and Planetary Science Letters 200 (2002) 315–330

EPSL

www.elsevier.com/locate/epsl

Quench rates in air, water, and liquid nitrogen, and inference of temperature in volcanic eruption columns

Zhengjiu Xu, Youxue Zhang *

Department of Geological Sciences, The University of Michigan, Ann Arbor, MI 48109-1063, USA

Received 23 January 2002; received in revised form 23 March 2002; accepted 5 April 2002

Abstract

We apply a geospeedometer previously developed in this lab to investigate cooling rate profiles of rhyolitic samples initially held at 720–750°C and quenched in water, liquid nitrogen, and air. For quench of mm-size samples in liquid nitrogen and in air, the cooling rate is uniform and is controlled by heat transfer in the quench medium instead of heat conduction in the sample. The heat transfer coefficient in 'static' air decreases with increasing sample size. For quench of mm-size samples in water, heat transfer in water is rapid and the cooling rate is largely controlled by heat conduction in the sample. Our experimental results are roughly consistent with previous calculations for cooling in air and in water (although constant heat transfer coefficients were used in these calculations), but cooling rate in liquid nitrogen is only 1.8–2.3 times that in 'static' air, and slower by a factor of 2 than calculated by previous authors. Cooling rate in compressed airflow is about the same as that in liquid nitrogen. The experimental results are applied to interpret cooling rates of pyroclasts in ash beds of the most recent eruptions of the Mono Craters. Cooling rates of pyroclasts are inversely correlated with sample size and slower than those in air. The results indicate that the hydrous species concentrations of the pyroclasts were frozen in the eruption column, rather than inside ash beds or in flight in ambient air. From the cooling rates, we infer eruption column temperature in a region where and at a time when hydrous species concentrations in a pyroclast were locked in. The temperature ranges from 260 to 570°C for the most recent eruptions of Mono Craters. These are the first estimates of temperatures in volcanic eruption columns. The ability to estimate cooling rates and eruption column temperatures from eruptive products will provide constraints to dynamic models for the eruption columns.

Keywords: water; air; nitrogen; cooling; Fourier Transform infrared spectroscopy; volcanism; eruptions

1. Introduction

As an eruption column ascends into the atmosphere, what is the temperature inside the column? When lava erupts in air, or when it enters water, what is the cooling rate? Some of these questions can be addressed using heat transfer models, but the accuracy of such models needs to be assessed and compared with measurements. Furthermore, quantification of experimental and natural cooling rates is critical for understanding sample behavior during quench, glass formation, volcanic eruption history, and thermal interaction between water and magma. Although it is well

* Corresponding author. Tel.: +1-734-763-0947; Fax: +1-734-763-4690.

E-mail addresses: zhengjiu@umich.edu (Z. Xu), youxue@umich.edu (Y. Zhang).

0012-821X/02/$ – see front matter
PII: S0012-821X(02)00656-8

known that quench rates vary with the quench medium, and are high in water and low in air (e.g., [1]), the only quantification of quench rates in different media was through calculation by solving heat transfer equations [2–5]. However, the accuracy of such calculations is not known because of the approximations (such as constant heat transfer coefficient) and because the complete physical problem including the effect of vapor formation and convection in the quench medium has not been solved. Hence cooling rates reported in the literature are often empirical (e.g., [6,7]) rather than based on calculations. Here we report the first experimental quantification of quench rate profiles in water, liquid nitrogen, and air based on an analytical technique previously developed in our laboratory [8–10]. We also determine cooling rates of pyroclasts as a function of their size, and compare these with cooling rates in air. Based on understanding gained from investigating cooling of pyroclasts and experimental charges, we report the first estimation of eruption column temperature in the part of the column where and at the time when hydrous species concentrations in pyroclasts were frozen in.

2. Principles and background for cooling rate determination

The method of cooling rate determination in this work is based on the kinetics of the interconversion reaction between molecular H_2O and OH groups in hydrous rhyolite [11], as measured by infrared (IR) spectroscopy [11–17]. We first explain the general principle of using kinetics of a homogeneous reaction (i.e., reaction between species in a single phase) to infer cooling rates. Because reaction rate increases with temperature, it takes a much shorter time to reach equilibrium at high temperature than at low temperature. Hence for a sample cooled from a high temperature at which equilibrium is rapidly reached, initially the species concentrations vary with temperature such that equilibrium is maintained as the temperature decreases. At some intermediate temperature, the species concentrations start to deviate from equilibrium. At still lower temperatures, the reaction effectively stops and species concentrations do not change any more. The final species concentrations in a phase when it is cooled to the ambient temperature hence depends on the cooling rate. If cooling is rapid, the sample stays for a shorter duration at each temperature interval and has less time to reach equilibrium. Therefore, the sample would only be able to reach equilibrium at a relatively high temperature, and the final species concentrations would reflect an apparent equilibrium at some high temperature. This temperature is called the apparent equilibrium temperature, referred to as T_{ae} [9,10,18–20]. Note that the sample did not reach equilibrium at the temperature of T_{ae} [20] (hence *apparent* equilibrium temperature). If cooling is slow, the final species concentrations would reflect an apparent equilibrium at a lower T_{ae}. Hence, T_{ae} is related to cooling rate: rapid cooling leads to a higher T_{ae}, and slow cooling leads to a lower T_{ae}. Therefore, if the equilibrium and kinetics of a homogeneous reaction are understood, the reaction can be used as a cooling rate indicator (or speedometer) [18–20].

The specific reaction employed in this work is the interconversion between molecular H_2O and OH groups in hydrous obsidian [8–11]. The composition of the obsidian is given in Table 1. Other pyroclasts investigated in this work have a similar composition [13]. The reaction can be written as:

$$H_2O\ (\text{melt}) + O^{2-}\ (\text{melt}) = 2OH^-\ (\text{melt}) \qquad (1)$$

where H_2O is a molecular H_2O (H_2O_m hereafter), O^{2-} is an anhydrous oxygen ion, and OH^- is a

Table 1
Chemical composition of the starting glass

Oxide	SiO_2	TiO_2	Al_2O_3	FeO	MgO	CaO	Na_2O	K_2O	H_2O	Total
wt%	75.91	0.06	12.51	0.99	0.03	0.54	4.00	4.75	0.82	99.61

Total H_2O concentration is from IR analyses and the rest are from electron microprobe analyses. The H_2O content in the sample is variable from 0.76% to 0.88% (see Table 3).

hydroxyl group in obsidian melt. The charges for O^{2-} and OH^- are ignored hereafter for simplicity. The two hydrous species can be distinguished in an IR spectrum. Molecular H_2O can be characterized by a vibrational combination band at 5230 cm^{-1}, and OH at 4520 cm^{-1}. From the intensity (i.e., absorbance) of each band, the concentrations of the hydrous species can be determined using Beer's law with calibration [11–17].

The equilibrium constant for the above reaction has been experimentally investigated extensively. At total H_2O content (H_2O_t) ≤ 2.5 wt% (it is 0.76–0.88 wt% for the sample used in this study), if the calibration of [13] is used, the equilibrium constant can be described by [13–15]:

$$K = \frac{[OH]^2}{[H_2O_m][O]} = \exp\left(1.876 - \frac{3110}{T}\right) \quad (2)$$

where [OH], [H_2O_m] and [O] represent molar fractions of the species on a single-oxygen basis [11,14], [O] = 1 − [H_2O_m] − [OH], and T is temperature in Kelvin. The dependence of K on pressure is negligible when pressure is less than 1.0 GPa [21]. For kinetic studies, the quotient Q (instead of the equilibrium constant K) is often used [8–10]:

$$Q \equiv \frac{[OH]^2}{[H_2O_m][O]} \quad (3)$$

Although the expression for Q is the same as that for K, K is for equilibrium only, and Q is used for reaction in progress or for apparent equilibrium. For a sample cooled from a high temperature, by measuring the final species concentrations, Q can be related to T_{ae} as follows (similar to Eq. 2):

$$Q = \exp(1.876 - 3110/T_{ae}) \quad (4)$$

In order to determine the relation between quotient Q and the cooling rate q, experimental calibration has been carried out in this laboratory [8–10]. Although the accuracy of measurements of IR band intensities is high, the molar absorptivities for converting band intensities to species concentrations still have some uncertainties [12–17]. To avoid unnecessary additional complexity and uncertainties in the calibration of the speedometer, the IR band intensities of the species are directly used instead of converting them to species concentrations [9,10]. Hence, the cooling rate can be calculated directly from an IR spectrum without knowing molar absorptivities. Although the anhydrous composition is fixed, the reaction rate depends strongly on the dissolved total H_2O content. Hence the procedure for obtaining q is complex and is as follows according to the newest calibration [10]. First, define:

$$Q' \equiv \bar{A}_{452}^2 / \bar{A}_{523} \quad (5)$$

where $\bar{A}_{452}$ and $\bar{A}_{523}$ are the linear absorbances of the IR bands at 4520 cm^{-1} and 5230 cm^{-1} per mm sample thickness, and Q' is a proxy for the quotient Q since $\bar{A}_{523}$ is roughly proportional to [H_2O_m] and $\bar{A}_{452}$ is roughly proportional to [OH]. From measured $\bar{A}_{452}$ and $\bar{A}_{523}$, the parameter ln$q$ and another dummy variable ξ are solved from the following two equations [10] by iteration:

$$y = 8.7905 + 7.8096\xi - 3.4937\xi^2 \quad (6)$$

$$\xi = \ln Q'|_{w=-1.7} = \ln Q' - f(w,y) + f(-1.7,y) \quad (7)$$

where $y = \ln q$, Q' is defined in Eq. 5, $w = \ln(\bar{A}_{452} + \bar{A}_{523})$, and $f(w,y) = -5.4276 - 1.196w - 0.044536y - 0.023054wy + 3.7339\exp(0.21361w + 0.030617y) - 0.37119\exp(1.6299w)$. More details can be found in [10]. A program written in Microsoft Excel to calculate the quench rate is available upon request from the corresponding author. The 2σ precision for calculating ln$q$ from the IR data is typically 0.2–0.3. The accuracy for ln$q$ is also 0.2–0.3 for the cooling rate range covered by the experimental calibration (0.00017–100 K s^{-1}) [10]. But beyond the calibrated cooling rate range, the accuracy is more difficult to assess. Nevertheless, some empirical rough estimate of the uncertainty is useful. Based on the small curvature of the best-fit curve (see figure 3 in [10]) over the q range of 0.00017–100 K s^{-1} (a factor of 600 000), we estimate the 2σ uncertainty in ln$q$ to be about 0.4 when q is extended outside the experimental data range in each direction by a factor of 2 (i.e., in the cooling rate range of 0.00008–0.00017 K s^{-1} and

of 100–200 K s^{-1}), about 0.5 when q is further extended outward by another factor of 2 (i.e., 0.00004–0.0008 K s^{-1}, or 200–400 K s^{-1}). The cooling rates investigated in this work range from 0.004 to 300 K s^{-1} (the greater cooling rates listed in Table 3 are only for limits and not used quantitatively).

During experimental or natural cooling, the instantaneous cooling rate in a given part of a sample may be variable with time (or temperature). In this case, the calculated cooling rate q from the IR spectrum is that when the sample temperature was the same as T_{ae} [20]. That is, the rigorous definition of q obtained by this method is

$$q = -\mathrm{d}T/\mathrm{d}t|_{T=T_{ae}} \quad (8)$$

3. Experimental and analytical procedures

Ten successful experiments were conducted on a natural hydrous rhyolitic glass KS and another Mono Crater pyroclast (Q1a in Table 2). The samples were chosen because the total H_2O content of $\sim$0.8 wt% is high enough for high-precision near-IR spectroscopic work of both H_2O_m (at 5230 cm^{-1}) and OH (at 4520 cm^{-1}) [11] and low enough to avoid significant bubbling during heating in an experiment. Although there is some heterogeneity in total H_2O content (see Table 3), it does not affect the results because the effect of total H_2O on the geospeedometer is well calibrated [9,10]. Table 2 lists experimental conditions, including the sample size. Three experiments were carried out using relatively large ($\geq$8 mm each side) and irregularly shaped glass chips, one each for cooling in water, liquid nitrogen, or air. In the other experiments, smaller pieces with more regular shapes (slices with thickness $<$5 mm) were used. Before each experiment, the piece of glass was prepared with at least one flat and polished surface. The experimental procedure generally followed that of [9,10] except for the quenching step. Each sample was heated to a temperature between 720 and 750°C for a prescribed duration in a one-atmosphere horizontal tube furnace and then quenched. This temperature was chosen as a compromise between the need to go to higher temperature so that greater cooling rates can be inferred (see later discussion) and the need to stay at lower temperature so as to minimize bubble growth. Some experiments were carried out at higher temperatures but the samples bubbled too much to be useful. For quenching in water or liquid nitrogen, the sample was rapidly pulled into a 1.0 or 2.0 l beaker of water or a 0.35 l dewar of liquid nitrogen. For quenching in room air (referred to as 'static' air although the air is not static because heating of air by the sample causes free convection), the sample was rapidly pulled into room air and held stationary by a

Table 2
Experimental conditions

Exp.	Sample size mm	L mm	T °C	Duration s	Quenching medium	Comment
Q5	$\sim$8×8×12	$\sim$1.5	748	300	1.0 liter water (room temp.)	a, b
Q10	3.963×10×10	1.105	750	450	2.0 liter water (room temp.)	a, b
Q6	$\sim$11.5×13×20	$\sim$2.3	751	600	0.35 liter liquid nitrogen (−196°C)	a, b
Q7	0.76×7×8	0.32	750	600	0.35 liter liquid nitrogen (−196°C)	b
Q1a	2.61×9×12	0.87	750	300	Air (room temp.)	
Q3	$\sim$8×8×8	$\sim$1.4	740	60	Air (room temp.)	
Q9	2.81×9.5×20	$\sim$1.0	727	300	Air (room temp.)	b
Q8	0.88×7×8	0.36	750	300	Air (room temp.)	b
Q12	4.81×13.06×13.83	1.40	720	300	Air (room temp.)	b
Q11	1.42×10.4×10.8	0.56	730	600	Airflow (room temp.)	b

The parameter L equals volume/(total surface area) and is the effective half thickness of the sample. T is the temperature right before quenching. Room temperature is about 21°C. Comments: a: the sample cracked; b: bubbles are present in quenched sample.

Table 3
Experimental results

x mm	A_{523}	A_{452}	d mm	H_2O_m wt%	OH wt%	H_2O_t wt%	T_{ae} °C	q K s^{-1}	q^* K s^{-1}
Q5 (quench in water)									
0.195	0.0346	0.192	1.328	0.111	0.689	0.800	753	> 618	
0.310	0.0352	0.1925	1.335	0.112	0.687	0.799	748	> 528	
0.363	0.0355	0.194	1.336	0.113	0.692	0.805	750	> 590	
0.502	0.0358	0.194	1.338	0.114	0.689	0.803	745	> 507	
0.603	0.0368	0.194	1.338	0.117	0.690	0.807	737	> 409	
0.697	0.0374	0.193	1.339	0.119	0.685	0.804	727	305	
0.954	0.0386	0.193	1.340	0.122	0.686	0.808	718	239	
1.313	0.0395	0.193	1.340	0.125	0.686	0.811	711	195	
1.49	0.0409	0.194	1.340	0.130	0.689	0.819	703	157	
1.83	0.0418	0.195	1.341	0.133	0.690	0.823	698	138	
1.91	0.0421	0.194	1.342	0.133	0.687	0.821	693	116	
2.54	0.0430	0.192	1.342	0.136	0.681	0.817	681	75	
3.30	0.0445	0.1932	1.337	0.142	0.686	0.828	675	65	
Q10 (quench in water); selected points									
0.411	0.0282	0.1467	0.979	0.123	0.718	0.840	747	> 646	
0.547	0.0289	0.1497	0.980	0.123	0.717	0.840	745	> 611	
0.98	0.0310	0.1464	0.985	0.134	0.710	0.844	711	238	
2.0 (center)	0.0324	0.1455	0.988	0.139	0.702	0.841	693	130	117
Quench in liquid nitrogen (all points with $x \leq 3.6$ mm in a given sample show similar cooling rates)									
Q6 ($x \leq 3.6$ mm; $n = 12$)				0.14	0.66	0.80	647	18	
Q6 (volume-averaged q of the whole sample)								14 (4–22)	
Q7 ($n = 3$)				0.141	0.714	0.855	700	174	396
Quench in air (all points in a given sample show similar cooling rates)									
Q8 ($n = 4$)				0.118	0.648	0.766	693	84	95
Q1a ($n = 5$)				0.103	0.578	0.68	665	17.8	
Q9 ($n = 4$)				0.145	0.660	0.805	646	20	
Q3 ($n = 9$)				0.18	0.70	0.88	624	12.7	
Q12 ($n = 7$)				0.164	0.672	0.836	622	8.7	21
Quench by blasting air onto the sample (all points show similar cooling rates)									
Q11 ($n = 4$)				0.125	0.660	0.784	688	79	

The variable x is the distance away from the pre-experimental polished surface. The number of analyses for each sample quenched in liquid nitrogen and air is given as n. A_{523} and A_{452} are the linear absorbances of the IR bands at 5230 cm^{-1} and 4520 cm^{-1}, respectively. Weight percents of H_2O_m (molecular H_2O), OH, and H_2O_t (total H_2O) are calculated from the calibration of [13]. T_{ae} is the apparent equilibrium temperature calculated from [13] using $\ln Q = 1.876 - 3110/T_{ae}$. The relative uncertainty in q is typically 20–30%, and is slightly worse for sample KS-Q10 because of many bubbles. Relative uncertainty for L may be as high as 30% for the irregularly shaped samples. For more regularly shaped samples, quench rates interpolated from the results of Birnie and Dyar [5] are also shown (as q^*).

thermocouple wire. In order to examine the role of airflow on quench rate, one sample is quenched by pulling it out of the furnace and blasting compressed 620 kPa (90 psi relative to ambient pressure) air onto the sample that is about 1 cm away from the nozzle.

Because of the stress induced during quenching, the water-quenched sample (Q5 and Q10) cracked slightly. The large sample (Q6) quenched in liquid nitrogen was held in liquid nitrogen for 30 min. After it was taken out of liquid nitrogen and when it was sitting on an alumina plate, it first cracked slightly with small cracking sounds, and then exploded into pieces, including six relatively large chunks. After solving the jigsaw puzzle of the pieces to pin down the relative position to the original polished surfaces, one piece with two originally polished surfaces was used for IR

work. Therefore, although cracking affected the preparation of the samples, it does not affect the reported results.

After quench, a wafer that is the most clear (free of bubbles and microlites) and close to the center of the sample was sectioned perpendicular to the original polished cooling surface. The wafer was then doubly polished. The doubly polished section was analyzed by a Fourier transform IR spectrometer. The earlier data were obtained with a Nicolet 60SX FTIR spectrometer, and more recent data are obtained with a Perkin-Elmer Spectrum GX FTIR spectrometer. The consistency between the two spectrometers has been verified. Although IR microscope measurement can be made with much higher spatial resolution, the difference between the microscope and main chamber IR analyses can be up to 5% relative. Hence for high-precision work in this study, IR microscope is not used.

The aperture used to limit the beam is typically a slit of 20 μm wide and 1 mm long. The slit is aligned parallel to the original quenching (polished) surface. The spatial resolution is about 30 μm using a 20 μm slit in the main chamber. The sample is moved so that IR spectra were taken as a function of distance from the original quenching surface. Bubble growth occurred for some samples during the experiment. Although efforts were made to avoid large bubbles in the IR beam path, the presence of bubbles lowered the accuracy of the analyses and caused some scatter for sample Q10, as will be seen in figures later. For other samples, the volume fraction of bubbles in the beam path is small and hence the measurement accuracy is not affected noticeably.

The baseline of the IR spectrum is fit by a flexicurve [12–14] and the peak heights are then obtained. Species and total H_2O concentrations are calculated from the peak height of 5230 cm^{-1} and 4520 cm^{-1} bands using the calibration of Zhang et al. [13]. This calibration is used because the calibration works well for this H_2O range (see also [14] for a review). The calibrations of Withers and Behrens [16] and of Nowak and Behrens [17] are mainly for converting high-temperature or low-temperature (below room temperature) in situ IR band intensities to species concentrations whereas our measurements are made at room temperature. Although Withers and Behrens [16] also included a calibration at 300 K measurement temperature, the calibration is for H_2O_t content above 2 wt%. Furthermore, to be consistent with the calibration of the geospeedometer [10], flexicurve baselines must be used.

Diffusion distances during the experiments are calculated from $(4Dt)^{1/2}$ (where t is the duration at the dwelling temperature of 720–750°C, D is diffusion-out diffusivity from [22], see also [23–25]) and are less than 50 μm. All the IR measurements are made at a distance greater than 50 μm away from the pre-experimental polished surface. Hence diffusion does not affect the results.

4. Results

Experimental results are summarized in Table 3. The IR band intensity data are used to calculate

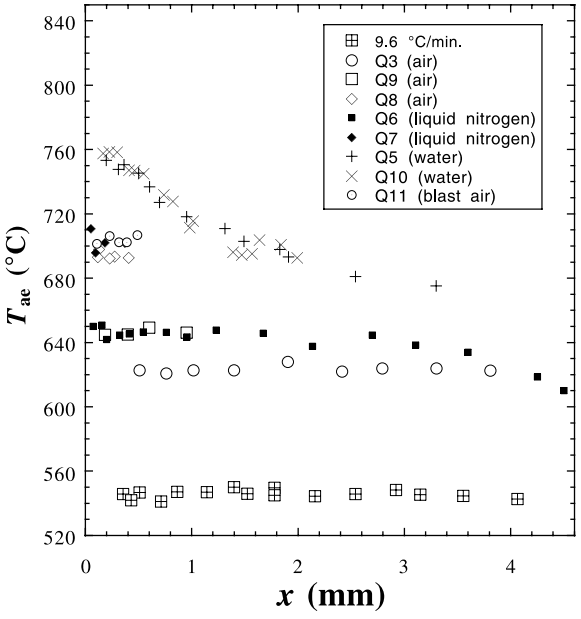

Fig. 1. The apparent equilibrium temperature as a function of distance from a quenching surface: data for quenching at constant rate of 0.16 K s^{-1} are from [9], and other data are from this work. Open symbols are for air quench, solid symbols for liquid nitrogen quench, and crosses for water quench. The apparent equilibrium temperature is calculated using the calibration of [13].

species concentrations [13], Q (using Eq. 3), apparent equilibrium temperature T_{ae} (using Eq. 4), Q' (using Eq. 5), and cooling rate q (iteration using Eqs. 6 and 7). Although T_{ae} is not needed for the calculation of the cooling rates with the procedure outlined above, it is necessary to know whether T_{ae} is close to the experimental temperature to interpret the calculated cooling rates.

The calculated T_{ae} values are shown in Table 3 and Fig. 1. As expected, T_{ae} depends on the quench medium. For quench in air and liquid nitrogen, T_{ae} depends on the sample size. For quench in water, T_{ae} depends on the distance away from the quench surface. In Fig. 1, T_{ae} at each point is plotted against the distance away from the quench surface. For reference, a sample cooled at a controlled cooling rate of 0.16 K s^{-1} from [9] is also shown. This sample has a uniform T_{ae} of 546 ± 5°C (2σ error hereafter) which does not vary with distance away from the quench surface (this distance is referred to as x) to the center ($x = 4.06$ mm). That is, at this slow cooling rate, interior cooling can keep pace with surface cooling because heat conduction in the sample is rapid enough for the sample size. For cooling in air, if the sample thickness is ≤ 8 mm, T_{ae} in each sample is also uniform, meaning that cooling is also slow enough for the interior to keep pace with surface cooling. Even though T_{ae} is uniform for a given sample, it decreases with increasing sample size and is 693 ± 5°C for a slab of 0.88 mm thickness, 647 ± 4°C for a slab of 2.83 mm thickness, and 623 ± 7°C for the 8 mm irregular piece (Fig. 1; Table 3). For cooling in liquid nitrogen, T_{ae} is uniform (700 ± 4°C) for a slab of 0.76 mm thickness, but for the larger sample, T_{ae} begins to show small changes as a function of distance away from the quench surface, from ~645°C near the cooling surface, to 630°C at $x = 3.8$ mm, to ~610°C at $x = 4.5$ mm (Fig. 1), indicating that for the larger sample, surface cooling rate is a little too high for cooling in the interior to keep pace. All of these observations are consistent with theoretical considerations discussed later.

For cooling in water, T_{ae} near the surface is the same as the experimental temperature 750°C, indicating that cooling at the surface is so rapid that the species concentrations at the experimental temperature are preserved. For two samples of different sizes (Q5 and Q10), T_{ae} vs. x curves are similar. At $x = 3.3$ mm, T_{ae} is 675°C, 75°C below the T_{ae} near the surface. Hence there is a large decrease in cooling rate as the distance from the cooling surface increases.

To calculate cooling rate from measured species concentrations, T_{ae} must be significantly less than the experimental temperature [9–11,18–20]. The relative error in the cooling rate calculation from the best IR data is 20–30%. If T_{ae} is the same as the experimental equilibrium temperature, it means that the cooling rate is high enough (greater than a critical value) to preserve the equilibrium at the experimental temperature. Under such conditions, cooling rate cannot be inferred quantitatively but the calculated q gives a lower limit. Numerical simulations using the method in [9,20] show that only when T_{ae} is less than the experimental temperature by ≥ 20°C, does q solved from species concentrations reflect actual cooling rate to within 20% relative. If one requires that q solved from species concentrations reflect actual cooling rate to within 1% relative, then T_{ae} must be at least 40°C less than the experimental temperature. However, because the uncertainty in obtaining q from IR band intensities is 20–30% relative, a 20°C difference is sufficient.

Fig. 2 shows q of all samples as a function of x. Cooling rates in water are much greater than those in air or liquid nitrogen because heat transfer in water is much more rapid. For samples quenched in air or liquid nitrogen, the cooling rate is uniform for a given sample as long as the half thickness is ≤ 4 mm. For different samples, the cooling rate is inversely related to the sample size, consistent with expectations (see Section 5). For cooling in water, q in a single sample decreases with increasing x. Within 0.5 mm of the surface, the quench rate is too high to be quantified. Nevertheless, a lower limit of q can be set. For example, at $x = 0.5$ mm, q is constrained to be > 500 K s^{-1}. That is, the quench rate for a small sample of 1 mm thick dropped into water is > 500 K s^{-1}. Further into the interior of the sample to 0.65 mm, the local quench rate becomes insufficient to preserve the species concentrations at the experimental temperature although the cal-

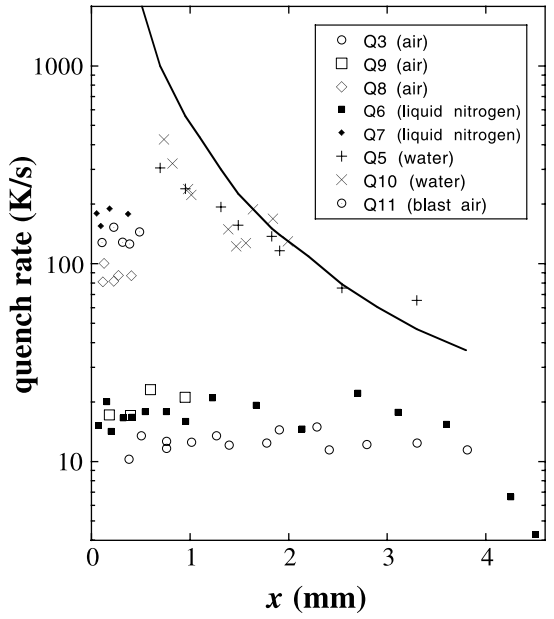

Fig. 2. Cooling rate profiles for samples quenched in air, liquid nitrogen and water. Symbols are the same as those in Fig. 1. The solid curve shows calculated maximum 1-D cooling rate in a sample as a function of distance away from the cooling surface (assumed to instantaneously cool to 25°C; i.e., $q=\infty$ at $x=0$). The greater cooling rate above the curve for water quench in the large sample (+ at $x=3.3$ mm) is believed to be due to cooling from other (irregular) surfaces.

culated cooling rates are still less than the actual cooling rate. For $x=0.7$ mm, the quench rate is $\sim$305 K s^{-1}. For $x=1$ mm, the quench rate is 220 K s^{-1}. For $x=3.3$ mm, the quench rate is about 65 K s^{-1}.

In summary, for quench in air or liquid nitrogen, q is roughly uniform for a given sample of ≤ 4 mm half thickness but decreases with increasing sample size, both of which indicate that quench rate is limited by heat transfer in air or liquid nitrogen, rather than by heat conduction in the obsidian. In contrast, for water quench, q decreases toward the sample interior in a given sample but q vs. x curves are similar for two samples of different sizes, both of which indicate that quench rate is mainly limited by heat conduction in the sample, rather than by heat transfer in water.

5. Discussion of experimental results

Theoretical models are available to treat cooling in air and in water. We will compare the results with three models, two of which are limiting models. In the first limiting model, heat conduction in the sample is much more rapid than heat transfer in the cooling medium (fluid). Thus the latter limits the cooling rate. In this model, the sample cooling rate is uniform from one point to another, hence called uniform cooling (also referred to as Newtonian cooling) [3]. In the second limiting model [2], heat conduction in the sample is much slower than heat transfer in the fluid. Thus the former limits the cooling rate. Assuming the surface temperature of the sample instantaneously becomes the fluid temperature (infinite q at the surface), this model constrains the maximum cooling rate of any solid in any fluid medium. The third model considers both heat transfer in the fluid and heat conduction in the sample assuming radiative heat loss at the surface [5]. No model explicitly considers the physical process of evaporation of a liquid quench medium and related complexities. The first model is roughly applicable to quench in air or liquid nitrogen as long as the half thickness of the sample is small enough. The second and third models are discussed in the context of quench in water.

5.1. *Uniform cooling model, and quench in air and liquid nitrogen*

Uniform cooling rates can be characterized as follows [3]:

$$q = -\mathrm{d}T/\mathrm{d}t|_{T=T_{ae}} = (T_{ae}-T_{ff})h/(\rho C_p L) \qquad (9)$$

where T_{ff} is the final fluid temperature (the temperature of the quench medium), h is the heat transfer coefficient of the fluid medium, ρ and C_p are the density and heat capacity of the sample to be cooled, and L is the effective half thickness and equals V/S where V and S are the volume and total surface area of the sample. Because the samples used in this study are mostly irregular in shape, estimated L has large uncertainties (diffi-

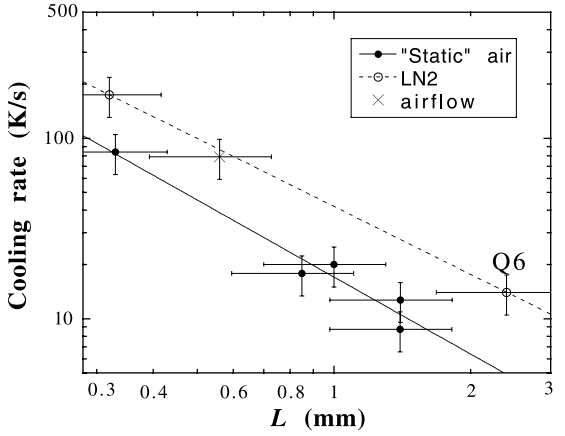

Fig. 3. Experimental cooling rates as a function of effective half thickness ($L = V/S$) for quench in 'static' air, liquid nitrogen and airflow. The error bars are nominal (30% relative for L, and 25% relative for quench rate). (The relative error for L is difficult to estimate, but for a few regularly shaped samples, the error bars are smaller than shown above.) The solid line is a regression line through the data for 'static' air. The dashed line is drawn through the two points for quench in liquid nitrogen. The slopes of the two lines are roughly the same, -1.4 ± 0.3.

cult to estimate but can reach 30% relative). Eq. 9 is applicable if $hL/k \leq 0.1$ [3], where k is thermal conductivity of the sample.

Fig. 3 shows the relation between q and L for samples cooled in 'static' air, liquid nitrogen, and airflow. The slopes on the log$q$ vs. log$L$ plot for cooling in 'static' air and liquid nitrogen are the same within uncertainty. The slope is -1.4 ± 0.3, steeper than -1 because in Eq. 9: (i) T_{ae} decreases with increasing L (Fig. 1), and (ii) h also decreases with increasing L ([26–30], and see below).

For rhyolitic glass, ignoring the temperature dependence, ρC_p is roughly $(2.7 \pm 0.3) \times 10^6$ J m^{-3} K^{-1} [31], and k is roughly 1.8 ± 0.2 W m^{-1} K^{-1} [32]. Because most samples are irregular in shape and some samples are very thin plates, the exact dependence of h on sample size is not known. Hence quantitative prediction of cooling rate from heat transfer consideration is not attempted. Instead, h can be calculated from Eq. 9 using the experimentally determined cooling rate.

For cooling in 'static' air, h is 111 W m^{-2} K^{-1} for Q8 ($L = 0.33$ mm), 65 W m^{-2} K^{-1} for Q1a ($L = 0.87$ mm), 86 W m^{-2} K^{-1} for Q9 ($L = 1.0$ mm), 80 W m^{-2} K^{-1} for Q3 ($L = 1.4$ mm), and 55 W m^{-2} K^{-1} for Q12 ($L = 1.40$ mm). Although there is scatter due to uncertainties in q and L, the heat transfer coefficient decreases with increasing sample size, consistent with the relation between Nusselt and Rayleigh numbers for cooling of spherical samples [26–30]. Using the average slope of -1.4 in Fig. 3, h (in W m^{-2} K^{-1}) in 'static' air can be expressed as $7.6/L^{1/3}$ where L is in m. Considering the uncertainty in L, the exponent of L may be as large as 1/2 (i.e., $h = 2.0/L^{1/2}$) or as small as 1/6. Taking into account of the dependence of h on the sample size, if $L \leq 3.5$ mm, the criterion $hL/k \leq 0.1$ for uniform cooling is roughly satisfied, consistent with observed uniform cooling rates. The h value of 138 W m^{-2} K^{-1}, determined by Birnie and Dyar [4], is similar to our results.

Fig. 3 shows that cooling rate in 620 kPa compressed air blast is about the same as that in liquid nitrogen, and is about two times that in 'static' air. Hence, h in 620 kPa compressed airflow is about two times that in 'static' air. On the other hand, h in liquid nitrogen calculated from Eq. 9 is 168 W m^{-2} K^{-1} for sample Q7 ($L \approx 0.32$ mm), and ~ 103 W m^{-2} K^{-1} for sample Q6 ($L \approx 2.3$ mm), about 1.5 times that in 'static' air and smaller than that in compressed airflow (note that part of the cooling rate difference is accounted for by the low temperature of liquid nitrogen). Thus, L must be ≤ 2 mm for uniform cooling. Hence sample Q6 is too large for uniform cooling, as shown by the experimental data themselves (Fig. 2). In order to plot sample Q6 in Fig. 3, the volume-averaged cooling rate of the whole sample is used instead of the constant cooling rate at $x \leq 3.6$ mm (Fig. 2, Table 3).

The heat transfer coefficient h of liquid nitrogen determined in this study is significantly smaller than 460 W m^{-2} K^{-1} determined by [4]. Although it is known that liquid nitrogen is not an effective quench medium, our data show that liquid nitrogen is a less efficient by a factor of ≥ 2 than previously calculated [4].

5.2. Half space cooling model and quench in water

Cooling in water is largely controlled by heat

conduction in the sample. For cooling in any quench medium, the maximum cooling rate inside a sample as a function of distance away from a cooling surface can be calculated assuming that the surface ($x=0$) cools instantaneously ($q=\infty$) to the final fluid temperature of 21°C. (In reality, it takes time for the surface to cool to the final fluid temperature.) With this assumption, for semi-infinite solid cooling in a fluid, the temperature inside the solid is [2]:

$$T = T_{ff} + (T_0 - T_{ff})\mathrm{erf}\left(\frac{x}{\sqrt{4\kappa t}}\right) \quad (10)$$

where T_{ff} is the ambient fluid temperature, T_0 is the initial temperature of the solid sample, x is the distance away from the cooling surface, κ is heat diffusivity of the sample, and t is time. The quench rate at a given position x is hence:

$$q = -\frac{dT}{dt}|_{T=T_{ae}} = \frac{(T_0 - T_{ff})}{\sqrt{4\pi\kappa t_{ae}^3}}\exp\left(-\frac{x^2}{4\kappa t_{ae}}\right) \quad (11)$$

where t_{ae} is the time when $T=T_{ae}$ at position x. The above equation gives the maximum cooling rate in a solid sample. The calculated maximum cooling rate is shown as the solid curve in Fig. 2. For small x, observed cooling rate is significantly smaller than the calculated maximum cooling rate, which is expected because surface cooling rate is not infinite. As x increases, the calculated maximum cooling rates and experimental cooling rates converge. At $x \approx 1$ mm, the maximum cooling rate inside the sample is about two times the cooling rate in water. When x increases further, the maximum cooling rate gets closer to the experimental cooling rate in water. That is, increasing the efficiency of cooling medium (such as using mercury) can increase cooling rates by at most a factor of two at the center of a sample thicker than 2 mm ($x>1$ mm), but may increase cooling rate more significantly closer to the surface, or for smaller samples.

Because a model assuming instantaneous cooling at the surface does not fit the experimental cooling rate profile well, one must consider both heat conduction in the rhyolite and heat transfer in water to treat the heat transfer problem. Birnie and Dyar [5] calculated quench rates at the center of a plate of infinite area with half thickness L by assuming constant h for a quench medium. As shown by previous authors [26–30] and earlier in this work, h depends on the sample size. Furthermore, our samples are not plates of infinite area. Hence we only compare experimental data from thin wafers (approaching the shape of plates) with calculated results (Table 3). There is fair agreement between some of our data and their calculation [5]. For example, for water quench, the experimentally determined q at the center of sample Q8 is 130 K s^{-1}, whereas the calculated q is 117 K s^{-1}. However, for quench in liquid nitrogen, the experimental cooling rate (174 K s^{-1}) is significantly less than the calculated cooling rate by Birnie and Dyar (396 K s^{-1}, Table 3), indicating that h of liquid nitrogen used by Birnie and Dyar [5] is not accurate.

6. Applications to cooling rate and temperature in eruption columns

During an explosive volcanic eruption, volcanic ash, pumice and pyroclasts are erupted high in the eruption column. Although thermal history of pyroclasts in an eruption column is complex, most pyroclasts cool more or less continuously in the eruption column (or pyroclastic flow), as they fly/fall through ambient air, and in volcanic beds after deposition. Cooling in eruption columns has been investigated through models and from color and magnetic mineralogy (e.g., [28,33–35]. The hydrous species geospeedometer can be applied to infer cooling rates of pyroclasts. From cooling rates, we may further infer where the pyroclasts cooled past T_{ae} as follows:

1. If they cooled past T_{ae} in volcanic beds after deposition, the cooling rate would be independent of clast size but dependent on the position in the beds (as shown by [36,37]).
2. If they cooled past T_{ae} in flight through ambient air, the cooling rate would be inversely correlated with clast size. Furthermore, they must have a cooling rate greater than that in 'static' air because airflow increases cooling rate as shown by sample Q11. The greater

the flight velocity, the greater the cooling rate [28].

3. If they cooled past T_{ae} in the eruption column with hot gas surrounding them, the cooling rate would also be inversely correlated with clast size. The cooling rate would be controlled by following two factors. One is the gas temperature in the eruption column (T_{ec}): a high gas temperature in the eruption column would lead to a low cooling rate (see Eq. 9 in which T_{ff} is equivalent to T_{ec}). The second is the free-fall velocity of the pyroclast through the column: a greater relative velocity leads to more rapid cooling. Because the temperature in the eruption column can be high, cooling rates of pyroclasts in eruption columns can be less then those in 'static' air.

Therefore, knowing how cooling rates of pyroclasts depend on clast size and whether cooling rates are less than in 'static' air, it is possible to determine where the pyroclasts cooled past T_{ae}. If they cooled past T_{ae} in the eruption column, it is further possible to infer the temperature in the part of the eruption column at the time when the pyroclast cooled past T_{ae}. That eruption column temperature will be referred to as T_{ec}, which is the final fluid temperature (T_{ff} in Eq. 9) for the cooling of the pyroclast and can be solved from Eq. 9. That is, the hydrous species geospeedometer provides estimate of eruption column conditions at which the species concentrations are frozen in.

Pyroclasts from the most recent eruption ($\sim$1340 AD) of Mono Craters, California, USA [38,39] are used to investigate cooling rates as a function of clast size ($L = V/S$). Sieh [38] has identified seven ash and lapilli air fall beds, representing different minor eruptions within several months. Pyroclasts from the beds were collected with the help of Blank and Dobson [8]. Although hundreds of pyroclasts from the collection have been analyzed over the years in this lab [8,10], the original size was not recorded. Thus, these cannot be used to examine whether q depends on L. Hence from the remaining pyroclasts, we selected those of different sizes for investigation. To determine the size (L) of a pyroclast when it cooled past T_{ae}, it is necessary to choose those that are not broken during collection. When the clasts are examined, some surfaces appear dull

Table 4
Results for pyroclasts

Sample No. #	Weight g	*a*, *b*, *c* mm	L mm	$\bar{A}_{523}$ mm^{-1}	$\bar{A}_{452}$ mm^{-1}	H_2O_t wt%	T_{ae} °C	q K s^{-1}	T_{ec} °C
2-N1	0.0426	2.2, 3.1, 5.5	0.423	0.0773	0.185	1.24	599	26	501 ± 33
2-N2	0.0836	3.1, 4.5, 5.5	0.538	0.235	0.267	2.37	531	55	256 ± 94
2-N4	0.1717	4.1, 4.5, 9.0	0.666	0.270	0.267	2.50	497	18	380 ± 40
2-N7	0.6014	5.5, 8.3, 12.0	1.014	0.176	0.232	1.91	526	11	407 ± 40
2-N9	1.9184	9.5, 13.0, 16.8	1.529	0.206	0.245	2.11	517	14	277 ± 81
2-N12	3.3121	13.0, 15.0, 15.5	1.881	0.258	0.251	2.35	478	4.2	384 ± 32
3-N1	0.0300	2.0, 2.0, 3.0	0.386	0.183	0.247	2.03	551	49	387 ± 56
3-N3	0.2382	3.5, 5.0, 5.0	0.771	0.123	0.213	1.58	565	22	395 ± 58
3-N4	0.7963	3.4, 9.5, 11.5	1.003	0.085	0.181	1.24	561	4.8	510 ± 17
5-N4	0.6225	5.8, 6.4, 8.5	1.064	0.122	0.206	1.54	546	7.8	458 ± 30
7-N5	0.2378	3.8, 5.4, 5.5	0.772	0.234	0.253	2.27	503	12	414 ± 30
7-N1	0.4472	5.6, 7.6, 9.4	0.941	0.0371	0.138	0.80	614	4.8	567 ± 16
7-N3	1.9200	9.0, 13.2, 16.0	1.520	0.086	0.149	1.07	468	0.004	N/A
7-N4[a]	8.9900	16.0, 18.5, 24.0	2.58	0.066	0.163	1.06	568*	1.7–4.4*	435 ± 49

The first digit of the sample number is the pyroclastic bed number. Some pyroclasts contain too low H_2O_t for cooling rates to be determined (analyzed but not shown here). For multiple analyses of the same sample, only the average is given (but in Fig. 4, individual analyses are plotted). Typical uncertainty is 0.0001 g for weight, about 20% relative for L, 1% relative for $\bar{A}_{523}$ and $\bar{A}_{452}$, 1% relative for H_2O_t, 5°C for T_{ae}, and 20–30% relative for q. Uncertainty for T_{ec} is estimated by propagating the uncertainty of q (25% relative), L (20% relative), ρC_p (10% relative), and ignoring the unknown uncertainty in h.

[a] [a]Sample 7-N4 is too large for uniform cooling. Hence q is more variable (see Fig. 4). Its T_{ec} is calculated from q near the surface of the pyroclast.

and original, and others show conchoidal fractures or are shiny. Pyroclasts with conchoidal or shiny surfaces are not used in this study since they might have been broken and might not reflect the original size. Because the clasts are irregular in shape, we use the following procedure to estimate L. Each pyroclast is weighed and the volume (V) is calculated using a density of 2320 kg m^{-3}. The pyroclast is treated as if it were a parallelepiped. The lengths of three dimensions (shortest, middle and longest) are measured as best as they can be, and are denoted as a, b, and c. If the clast were a rectangular parallelepiped, L would equal to: $abc/[2(ab+ac+bc)]$. Because the clast has irregular shape and because the volume V is known with good accuracy, we obtain L by adjusting the above as:

$$L = \frac{abc}{2(ab+ac+bc)}\sqrt[3]{\frac{V}{abc}} \tag{12}$$

That is, we assume that the measured length is off by a constant factor of $[V/(abc)]^{1/3}$. Although the procedure is not perfect, we estimate that L is accurate to within 20% relative.

A wafer is sectioned from the middle part of each pyroclast, and doubly polished for IR analyses. For large samples, several points are measured from rim to the center of the clast to assess variation of cooling rate. From the IR analyses, T_{ae} and q are calculated. The results are reported in Table 4. The cooling rate is plotted against pyroclast size in Fig. 4 except for one pyroclast (7-N3) that is outside the figure and will be discussed later. Although there is some scatter, Fig. 4 shows that: (i) most pyroclasts have cooling rates below those in 'static' 21°C air, and (ii) the cooling rates of the pyroclasts decrease with L, following a trend that is sub-parallel to that in 'static' air. Hence, the pyroclasts must have cooled past T_{ae} in hot gas inside the volcanic eruption column, not in the ambient air, nor in the ash beds.

Knowing that the pyroclasts cooled past T_{ae} in the eruption column, we can use Eq. 9 to estimate the gas temperature in the eruption column if the heat transfer coefficient h in the eruption gas column is known. We estimate h by considering forced convection due to the free fall of a pyroclast. Because theory for motion and heat transfer of an irregularly shaped particle through a fluid is not available, we treat a pyroclast as a sphere of equal volume. First the freefall velocity u and the Reynolds number Re are estimated through iteration as follows [26]:

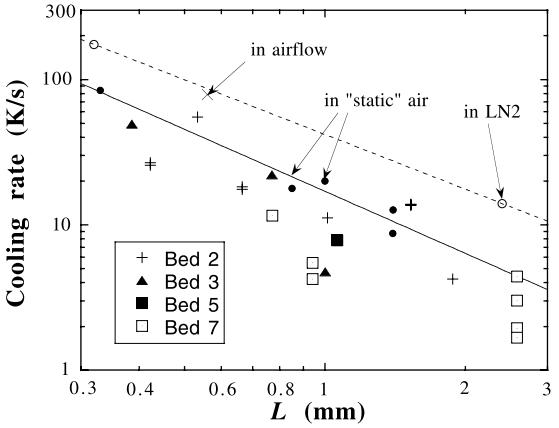

Fig. 4. Cooling rates as a function of effective half thickness (L) for pyroclasts in ash beds of the most recent eruptions of Mono Craters [37]. For comparison, the data and lines from Fig. 3 for experimental cooling in air (solid circle and solid line), liquid nitrogen (open circles and dashed line), and air blast ($\times$) are shown using the same symbols as in Fig. 3. Typical 2σ error in determining q is about 20–30% relative. Large pyroclasts such as sample 7-N4 (with $L = 2.58$ mm) have variable cooling rate (1.7–4.4 K s^{-1}; four dotted squares at $L = 2.58$ mm) from interior to the surface. One clast ($L = 1.52$ mm) in Bed 7 has very low cooling rate ($q \approx 0.004$ K s^{-1}) and is not shown in this figure.

$$\mathrm{Re} = \frac{ud\rho_{air}}{\mu} \tag{13a}$$

$$C_D = \frac{24}{\mathrm{Re}}(1 + 0.15\mathrm{Re}^{0.687}) + \frac{0.42}{1 + 42500\mathrm{Re}^{-1.16}} \tag{13b}$$

$$u = \sqrt{\frac{4gd\rho_s}{3\rho_{air}C_D}} \tag{13c}$$

where d is the diameter of the sphere, ρ_{air} is the air density, μ is the viscosity of air, C_D is the drag coefficient, ρ_s is the pyroclast density, and g is acceleration due to Earth's gravity. Eq. 13b is

from [26] and the relative error is +6% to −4% for Re $<3\times10^5$. An approximate equation for u is $u=1.73(gd\rho_s/\rho_{air})^{1/2}$ [26]. Then the Nusselt number is estimated. Because Re is between 100 and 3×10^5, the Nusselt number is calculated using the following relation [40]:

$$\mathrm{Nu}\equiv hd/k = 2 + (0.25\mathrm{Re} + 0.0003\mathrm{Re}^{1.6})^{1/2} \quad (14)$$

where k is thermal conductivity of air. Note that Thomas and Sparks [28] misquoted the above equation (0.25Re was misquoted as 0.25). From Nu, the heat transfer coefficient is obtained as follows:

$$h\equiv \mathrm{Nu}(k/d) \quad (15)$$

Although air density, viscosity and thermal conductivity depend on air temperature, the value of h only varies by about 26% from 300 to 800 K. Hence a constant temperature of 700 K is used for air temperature in the eruption column for estimating h. The value of h thus obtained depends on the size of the clast, varying from 315 W m^{-2} K^{-1} for a clast of 3 mm diameter to 215 W m^{-2} K^{-1} for a clast of 20 mm diameter, significantly greater than h values in 'static' air, as expected.

Knowing h, the eruption column temperature T_{ec} as each pyroclast cooled past T_{ae} is calculated using Eq. 9 and shown in Table 4. For eruption 2 (the eruption that resulted in Bed 2), the eruption column temperature recorded by the pyroclasts ranges from 256 to 501°C. For eruption 3, the eruption column temperature ranges from 387 to 510°C. For eruption 7, the eruption column temperature ranges from 414 to 567°C. For pyroclasts previously analyzed in this lab [8,10], although their sizes were not determined, most of them have cooling rates in the same range of 2–50 K s^{-1}, consistent with cooling past T_{ae} in the eruption column with similar eruption column temperatures. Even though the accuracy of the calculation is not known due to uncertainties in estimating h for irregularly shaped pyroclasts, these are reasonable temperatures for eruption columns.

The meaning of the calculated temperatures in the eruption columns is as follows. Temperature in an eruption column as air is mixed into the column is obviously variable with both space and time. The gas temperature T_{ec} experienced by a given pyroclast indicates the average gas temperature when it cooled from T_{ae} +40°C to T_{ae} −40°C. (Above T_{ae} +40°C, there was roughly continuous equilibrium; below T_{ae} −40°C, the reaction effectively stopped. The choice of ±40°C depends on measurement precision). Using cooling rates in Fig. 4, the smallest pyroclast cooled through this 80°C temperature interval in 2 s, and the largest one cooled through this temperature interval in ~40 s. (The exception of one pyroclast with very low cooling rate will be discussed below.) Hence, although each pyroclast cooled more or less continuously in an eruption column from a temperature greater than T_{ae} to a much lower temperature (some of the cooling was after deposition), the estimated T_{ec} from each pyroclast means the gas temperature in the part of the eruption column during the time interval (of 2–40 s) when the pyroclast was cooling from T_{ae} +40°C to T_{ae} −40°C.

In comparison, inferred emplacement temperature for the 18 May 1980 deposits of Mount St. Helens is 330, 240 and 110°C for three sites at 6.5, 5, and 9.5 km away from the crater [41]. These low temperatures cannot reset the hydrous species concentrations in a reasonable amount of time (days to months) and hence cannot be recorded by the hydrous species geospeedometer. (At 330°C, if H_2O concentration is high enough, hydrous species concentrations can be reset in days to months.) Obviously, temperature in eruption columns depends on many factors, including the size of the eruption, the clast to gas ratio, the amount of ambient air that is mixed into the column, the distance away from the eruption vent, and height in the column, etc.

We now turn to sample 7-N3 in Bed 7 (Table 4). Its very low cooling rate (0.004 K s^{-1}, 1000-fold lower than the expected cooling rate) is puzzling. Among the hundreds of pyroclasts from this site that were measured in our lab before (although L was not determined for those analyzed earlier [8,10]) and samples analyzed in this study, sample 7-N3 is the only sample with such a low cooling

rate. All the other pyroclasts have much greater cooling rates; most of them have cooling rates between 1 and 60 K s^{-1} [10], similar to those shown in Fig. 4. One explanation for the low cooling rate is that the pyroclast cooled past T_{ae} in the conduit prior to the eruption and was not heated up enough during the eruption that brought it up [8,10,39]. Noting that T_{ae} of this sample (468°C) is not high compared to the eruption column temperature of 414–567°C, an alternative explanation for the cooling history of the sample is as follows. The pyroclast might have cooled in a relatively hot region in the eruption column (such as 550°C) and hence did not cool below its apparent equilibrium temperature. That is, the sample was still hot enough (such as 550°C) for the hydrous species reaction to go on when it landed in the ash bed. Then the sample was buried in the bed and cooled slowly in the bed at a rate of 0.004 K s^{-1} (350 K day^{-1}). Hence the very low cooling rate can be explained by cooling through T_{ae} in the ash bed.

The above results show that the hydrous species geospeedometer and the characterization of cooling rates in air can be applied to understand the rich details of volcanic eruption columns. Other cooling rate indicators (e.g., [35]) may also be applied the same way if they can be quantified to predict cooling rates to within a factor of two. In addition, our geospeedometer can be applied to infer cooling rates of volcanic glasses and thermal history in pumice deposit [36], to investigate thermal interaction between water and magma to understand the conditions for hydrovolcanism [42,43], to refine heat transfer models by comparing directly measured cooling rates with theoretical calculations, and to determine heat transfer coefficients in a fluid medium under various conditions.

7. Summary

1. The uniform cooling model works well for cooling in air and liquid nitrogen, as long as the effective half thickness is ≤ 4 mm. Cooling rate of an obsidian with an effective thickness of 1 mm is about 20 K s^{-1} in 'static' air, and decreases with increasing sample size. Cooling rates in 620 kPa compressed airflow and in liquid nitrogen are about two times those in 'static' air. Liquid nitrogen is a less efficient quench medium than previously thought.
2. Our experimental approach provides a method for determining the heat transfer coefficient of a quench medium. The heat transfer coefficient for 'static' air and liquid nitrogen decreases with the size of the sample to be cooled, consistent with predictions. The heat transfer coefficient for liquid nitrogen for a spherical sample with radius of 1 mm is only 40% of the reported 460 J K^{-1} m^{-2} s^{-1} [4].
3. Cooling rate in water is ≥ 500 K s^{-1} for a sample ≤ 1 mm thick. Cooling rate of a sample in water varies with distance away from the cooling surface and this cooling rate vs. distance relation is the same for large and small samples. To model cooling rate in water, one has to consider both heat conduction in the solid sample and heat transfer in water.
4. Although our experiments are conducted using hydrous obsidian, the cooling rates obtained here are applicable to all materials having heat transfer properties similar to those of rhyolite. Because heat diffusivity and conductivity do not vary widely from one material to another, the above results are applicable to most materials as long as the volume ratio of the quench medium to the sample is large.
5. Our results on cooling rates in 'static' air provide a baseline for understanding cooling rates of pyroclasts. Cooling rates of pyroclasts collected from volcanic beds of the most recent eruption of Mono Craters are smaller than those in 'static' air and are inversely correlated with pyroclast size, indicating that they cooled past T_{ae} in the eruption column. Inferred temperatures in three eruption columns range from 256 to 567°C. These applications show the power of the hydrous species geospeedometer in revealing rich details of volcanic processes.

Acknowledgements

We thank Harald Behrens, Steve Sparks, Bruce

Watson, Jiba Ganguly, Eric Essene, and Henry Pollack for reviewing this manuscript, and M.D. Dyar for pointing out references that we missed. We also thank Jim Windak for helping with FTIR maintenance and operation. This work is funded by NSF Grants EAR-9706107, EAR-9972937, EAR-0125506.*[BW]*

References

[1] M.D. Dyar, D.P. Birnie III, Quench media effects on iron partitioning and ordering in lunar glass, J. Non-Cryst. Solids 67 (1984) 397–412.
[2] H.S. Carslaw, J.C. Jaeger, Conduction of Heat in Solids, Clarendon Press, Oxford, 1959, 510 pp.
[3] G.H. Geiger, D.R. Poirier, Transport Phenomena in Matallurgy, Addison-Wesley, Reading, MA, 1973, 616 pp.
[4] D.P. Birnie, W.D. Kingery, Quenching of solid samples for high temperature equilibrium measurement, J. Mater. Sci. 20 (1985) 2193–2198.
[5] D.P. Birnie, M.D. Dyar, Cooling rate calculations for silicate glasses, J. Geophys. Res. 91 (1986) D509–D513.
[6] L. Silver, P.D. Ihinger, E. Stolper, The influence of bulk composition on the speciation of water in silicate glasses, Contrib. Mineral. Petrol. 104 (1990) 142–162.
[7] D.B. Dingwell, S.L. Webb, Relaxation in silicate melts, Eur. J. Mineral. 2 (1990) 427–449.
[8] Y. Zhang, E.M. Stolper, P.D. Ihinger, Kinetics of reaction $H_2O+O=2OH$ in rhyolitic glasses: preliminary results, Am. Mineral. 80 (1995) 593–612.
[9] Y. Zhang, J. Jenkins, Z. Xu, Kinetics of the reaction $H_2O+O=2OH$ in rhyolitic glasses upon cooling: geospeedometry and comparison with glass transition, Geochim. Cosmochim. Acta 61 (1997) 2167–2173.
[10] Y. Zhang, Z. Xu, H. Behrens, Hydrous species geospeedometer in rhyolite: improved calibration and application, Geochim. Cosmochim. Acta 64 (2000) 3347–3355.
[11] E. Stolper, The speciation of water in silicate melts, Geochim. Cosmochim. Acta 46 (1982) 2609–2620.
[12] S. Newman, E.M. Stolper, S. Epstein, Measurement of water in rhyolitic glasses: calibration of an infrared spectroscopic technique, Am. Mineral. 71 (1986) 1527–1541.
[13] Y. Zhang, R. Belcher, P.D. Ihinger, L. Wang, Z. Xu, S. Newman, New calibration of infrared measurement of water in rhyolitic glasses, Geochim. Cosmochim. Acta 61 (1997) 3089–3100.
[14] Y. Zhang, H_2O in rhyolitic glasses and melts: measurement, speciation, solubility, and diffusion, Rev. Geophys. 37 (1999) 493–516.
[15] P.D. Ihinger, Y. Zhang, E.M. Stolper, The speciation of dissolved water in rhyolitic melt, Geochim. Cosmochim. Acta 63 (1999) 3567–3578.
[16] A.C. Withers, H. Behrens, Temperature-induced changes in the NIR spectra of hydrous albitic and rhyolitic glasses between 300 and 100 K, Phys. Chem. Miner. 27 (1999) 119–132.
[17] M. Nowak, H. Behrens, Water in rhyolitic magmas: getting a grip on a slippery problem, Earth Planet. Sci. Lett. 184 (2001) 515–522.
[18] R.F. Mueller, Kinetics and thermodynamics of intracrystalline distributions, Mineral. Soc. Am. Spec. Pap. 2 (1967) 83–93.
[19] J. Ganguly, Mg-Fe order-disorder in ferromagnesian silicates II: thermodynamics, kinetics and geological applications. In: S.K. Saxena (Ed.), Advances in Physical Geochemistry, vol. 2, Springer-Verlag, New York, 1982, pp. 58–99.
[20] Y. Zhang, Reaction kinetics, geospeedometry, and relaxation theory, Earth Planet. Sci. Lett. 122 (1994) 373–391.
[21] Y. Zhang, Pressure dependence of the speciation of water in rhyolitic glasses, EOS 74F (1993) 631.
[22] Y. Zhang, E.M. Stolper, G.J. Wasserburg, Diffusion of water in rhyolitic glasses, Geochim. Cosmochim. Acta 55 (1991) 441–456.
[23] Y. Zhang, E.M. Stolper, G.J. Wasserburg, Diffusion of a multi-species component and its role in the diffusion of water and oxygen in silicates, Earth Planet. Sci. Lett. 103 (1991) 228–240.
[24] Y. Zhang, H. Behrens, H_2O diffusion in rhyolitic melts and glasses, Chem. Geol. (Wasserburg volume) 169 (2000) 243–262.
[25] L. Wang, Y. Zhang, E.J. Essene, Diffusion of the hydrous component in pyrope, Am. Mineral. 81 (1996) 706–718.
[26] R. Clift, J.R. Grace, M.E. Weber, Bubbles, Drops, and Particles, Academic Press, New York, 1978, 380 pp.
[27] K. Jafarpur, M.M. Yovanovich, Laminar free convective heat transfer from isothermal spheres: a new analytical method, Int. J. Heat Mass Transfer 35 (1992) 2195–2201.
[28] R.M.E. Thomas, R.S.J. Sparks, Cooling of tephra during fallout from eruption columns, Bull. Volcanol. 54 (1992) 542–553.
[29] R.C. Kerr, Convective crystal dissolution, Contrib. Mineral. Petrol. 121 (1995) 237–246.
[30] P. McLeod, R.S.J. Sparks, The dynamics of xenolith assimilation, Contrib. Mineral. Petrol. 132 (1998) 21–33.
[31] R.A. Lange, The effect of H_2O, CO_2 and F on the density and viscosity of silicate melts, Reviews in Mineralogy 30 (1994) 331–369.
[32] C. Clauser, E. Huenges, Thermal conductivity of rocks and minerals, in: T.J. Ahrens (Ed.), AGU Reference Shelf 3: Rock Physics and Phase Relations, vol. 3, AGU, Washington, DC, 1995, pp. 105–126.
[33] J. Marti, J.L. Diez-Gil, R. Ortiz, Conduction model for the thermal influence of lithic clasts in mixtures of hot gases and ejecta, J. Geophys. Res. 96 (1991) 21879–21885.
[34] M. Hort, J. Gardner, Constraints on cooling and degassing of pumice during plinian volcanic eruptions based on model calculations, J. Geophys. Res. 105 (2000) 25981–26001.
[35] S. Tait, R. Thomas, J. Gardner, C. Jaupart, Constraints

on cooling rates and permeabilities of pumices in an explosive eruption jet from colour and magnetic mineralogy, J. Volcanol. Geotherm. Res. 86 (1998) 79–91.
[36] A.T. Anderson, P. Wallace, Cooling rates of rhyolitic glass inclusions from the Bishop Tuff, EOS 81 (2000) S439.
[37] P.J. Wallace, J. Dufek, A.T. Anderson, Cooling rates of plinian-fall and pyroclastic flow deposits in the Bishop Tuff: Inferences from water speciation in quartz-hosted glass inclusions, J. Petrol. 2001 (submitted).
[38] K. Sieh, M. Bursik, Most recent eruptions of the Mono Craters, eastern central California, J. Geophys. Res. 91 (1986) 12539–12571.
[39] S. Newman, S. Epstein, E.M. Stolper, Water, carbon dioxide, and hydrogen isotopes in glasses from the ca. 1340 A.D. eruption of the Mono Craters, California: Constraints on degassing phenomena and initial volatile content, J. Volcanol. Geotherm. Res. 35 (1988) 75–96.
[40] E. Achenbach, Heat transfer from spheres up to $Re = 6\times10^6$, Proc. Sixth Int. Heat Transfer Conf. 5 (1978) 341–346.
[41] M.P. Ryan, N.G. Banks, R.P. Hoblitt, J.Y.K. Blevins, The *in-situ* thermal transport properties and the thermal structure of Mount St Helens eruptive units, in: M.P. Ryan (Ed.), Magma Transport and Storage, Wiley, New York, 1990, pp. 137–155.
[42] R.S.J. Sparks, M.I. Bursik, S.N. Carey, J.S. Gilbert, L.S. Glaze, H. Sigurdsson, A.W. Woods, Volcanic Plumes, Wiley and Sons, New York, 1999, 574 pp.
[43] B. Zimanowski, R. Buttner, V. Lorenz, H.-G. Hafele, Fragmentation of basaltic melt in the course of explosive volcanism, J. Geophys. Res. 102 (1997) 803–814.